Watt-class CMOS-compatible optical high power amplifier

Neetesh Singh

neeteshs85@gmail.com

DESY https://orcid.org/0000-0001-9105-647X

Jan Lorenzen

Deutsches Elektronen-Synchrotron https://orcid.org/0009-0008-6058-2002

Kai Wang

University of Twente https://orcid.org/0009-0007-4912-4652

Mahmoud Gaafar

Deutsches Elektronen-Synchrotron

Milan Sinobad

Deutsches Elektronen-Synchrotron https://orcid.org/0000-0003-3490-0288

Henry Francis

LIGENTEC

Marvin Edelmann

Deutsches Elektronen-Synchrotron

Michael Geiselmann

LIGENTEC

Tobias Herr

Deutsches Elektronen-Synchrotron

Sonia Garcia-Blanco

University of Twente

Franz Kärtner

Center for Free-Electron Laser Science - CFEL, Deutsches Elektronen-Synchrotron - DESY / Universität Hamburg https://orcid.org/0000-0001-8829-5461

Article

Keywords:

Posted Date: June 25th, 2024

DOI: https://doi.org/10.21203/rs.3.rs-4602013/v1

Additional Declarations: There is **NO** Competing Interest.

Abstract

High power amplifiers are critical components in optical systems spanning from long range optical sensing and optical communication systems to micromachining and medical surgery. Today, integrated photonics with its promise of large reductions in size, weight and cost cannot be used in these applications, due to the lack of on-chip high power amplifiers. Integrated devices severely lack in output power due to their small size which limits energy storage capacity. For the last two decades, large mode area (LMA) technology has played a disruptive role in fiber amplifiers enabling a dramatic increase of output power and energy by orders of magnitude. Thanks to the capability of LMA fiber to support significantly larger optical modes the energy storage and power handling capability has significantly increased. Therefore, an LMA device on an integrated platform can play a similar role in power and energy scaling of integrated devices. In this work, we demonstrate LMA waveguide-based CMOS compatible watt-class high power amplifiers with an on-chip output power reaching beyond ~ 1 W within a footprint of only ~ 4 mm^2. The power achieved is comparable and even surpasses many fiber-based amplifiers. We believe this work has the potential to radically change the integrated photonics application landscape, allowing power levels previously unimaginable from an integrated device replacing much of today's benchtop systems. Moreover, mass producibility, reduced size, weight and cost will enable yet unforeseen applications for laser technology.

Introduction

High power amplifiers are usually associated with solid-state and fiber-based bench top systems. That is due to the large energy storage capacity of such systems, owing to the large optical mode cross section, gain area and the long cavity length. High power amplifiers find a variety of applications such as in amplifying low noise mode-locked laser pulses, CW laser signals, in high power optical frequency comb generation, spectroscopy, laser detection and ranging, telecommunication (pre-amp, in-line and booster amplifiers), materials processing and medical applications to name a few [1-15]. Benchtop high power amplifiers are a necessity for many photonic systems, but as we move towards system level miniaturization [11-13], and applications in hostile environments – such as deep space, their size and weight become a major roadblock as they are hard to scale down and mass produce [11-20].

Fiber amplifiers and semiconductor amplifiers, which can be electrically pumped, have been quite successful in the telecommunication industry and other applications. Semiconductor high power amplifiers, and in particular slab coupled optical waveguide amplifiers have shown watt-level amplification in the telecom window [21]; however, so far their photonic integration has met with challenges. There are semiconductor amplifiers that can be heterogeneously integrated. However, not only the amplified power is merely in the 10s of mW range due to high thermal instability and nonlinear absorption loss [22-25], yield and integration cost is still a concern, especially with silicon photonics as the lattice mismatch between silicon and III-V semiconductor materials hinders epitaxial growth, requiring expensive techniques such as flip-chip and wafer-level bonding; however, progress is being made [22, 25].

Rare-earth gain ions, thanks to the shielding of the 4f shell, are relatively unaffected by their host environment and exhibit rich optical spectra while being barely affected by thermal instabilities and nonlinear losses. Hence, it's not surprising that most high power solid-state and fiber amplifiers and lasers are based on rare-earth-doped gain media. In fact, due to these excellent qualities rare-earth doped semiconductor devices were investigated even before the erbium-doped-fiber-amplifier (EDFA) was invented [26-28]. Over the last two decades, rare-earth gain media have been satisfactorily demonstrated at chip scale [29-42]. However, the output power from these devices has remained low. Very recently amplification up to 140 mW in the C-band with very long low-loss erbium doped silicon nitride waveguides was demonstrated [42]. However, that was at the expense of a complex fabrication process, and there remain concerns about instabilities from nonlinear effects at high power (just like in fibers with long lengths and tight mode confinement), and multi-modedness which can lead to loss of energy to unwanted modes [5]. For high power applications it is desirable to have a shorter device that supports a large optical mode and gain region [43-46], which increases the gain saturation power and helps to reduce nonlinear effects while at the same time increases the energy storage capacity. In integrated photonics, however, the very property of tight mode confinement, that enables a small form factor, becomes an impediment to high power and energy applications, limiting the power to a few 10s of mW [22-24], and only a few mWs in the mid-infrared window [47]. We have recently explored a CMOS compatible large-mode-area (LMA) waveguide for integrated photonics [48, 49]. Such an LMA waveguide helps to increase the energy storage capacity and gain saturation power while incurring negligible nonlinear instabilities, and all that within a compact footprint. In this work, we leverage on such an LMA technology and demonstrate for the first time a CMOS compatible *watt*-class high power amplifier with signal amplification reaching up to ~1 W in a compact footprint of 4.4 mm^2 (0.2x21 mm). The signal power reaches and even surpasses the level enjoyed by many commercial bench top fiber amplifiers [50, 51]. The LMA device supports mode area in the range of 10s of μm^2 increasing the gain saturation power comparable to high power fiber amplifiers. Moreover, unlike an LMA fiber amplifier, the on-chip LMA device supports only fundamental mode propagation, tight bends, easy interfacing with different photonic components, and high pump and signal mode overlap even when they are spectrally quite far apart.

Design and experiments

The gain waveguide cross-section is shown in Fig. 1a, where an active layer is on top of a passive layer. Devices based on an active layer on top of a passive have been explored before for signal gain and modulation [52-55]. Semiconductor gain [52-54] and rare-earth gain media [29, 40, 56] have been implemented in this manner; however, due mainly to small mode area the power has remained low. Here we introduce large mode area gain layer while maintaining a compact footprint. Here, the gain waveguide consists mainly of a bottom silicon nitride (SiN) layer buried in silica and a top gain layer. The SiN thickness can vary depending on the wavelength of interest and the foundry of fabrication, allowing flexible fabrication at different CMOS foundries. For the proof of principle demonstration, we chose thulium doped aluminum oxide gain medium (Tm^{3+}:Al_2O_3) due to ease in availability and various mid-

infrared medical and defense applications [57-61]. The thickness of the gain layer is >1.35 μm on top of a silica cladding layer within which a 800 nm thick SiN layer is buried (such a thick SiN allows seamless integration to conventional nonlinear photonics components). The SiN layer was designed to have a width (w) and the interlayer oxide thickness (g) of around 280 nm and 310 nm, respectively.

The simulated TM mode profile of the signal is shown in Fig. 1b, having a pump and signal mode overlap of >98%. The mode area is ~ 30 μm^2 around the signal (1.85 μm) and 31 μm^2 around the pump (1.61 μm) wavelength. The signal and pump mode overlap with the gain layer is 92% and 94%, respectively. A schematic of the LMA amplifier is shown in Fig. 1c. The LMA gain sections are the straight sections within the gain deposited region (enclosed with the green box). To obtain a compact footprint these gain sections are interconnected with each other with the help of tight bends in which the large modes from the LMA sections are transitioned into the small modes (~1.5 μm^2 mode area) through adiabatic tapers, shown as brown lines. The length of the gain section is ~ 6.2 cm. For pumping the gain medium, we chose an in-band pumping scheme. Such a scheme helps to reduce quantum defect (the difference in the pump and the signal photon energy), and thus helps to improve conversion efficiency [62-64] and allows for a relaxed choice of pump wavelength which can be within the range from 1.55 μm to 1.7 μm for thulium doped aluminum oxide. A simplified energy diagram is shown in Fig. 1d showing the upper and lower energy level manifolds. The signal generation can span from 1750 nm to beyond 2 μm [62], thanks to the broadband gain bandwidth of thulium doped glass.

The device was fabricated in a silicon photonics foundry on a silicon-nitride-on-silicon platform. The thickness of the SiN layer is 800 nm (thinner layers that are commonly available in a CMOS facility can equally be applied with minor modification of the waveguide cross-section). The photonic stack consists of a layer of silicon, bottom silicon, bottom silicon dioxide, silicon nitride (800 nm thick), top silicon dioxide and the gain aluminum oxide layer. A gain layer (Tm^{3+}:Al_2O_3) of >1.35 μm thickness is deposited with a radio-frequency (RF) sputtering tool at a rate of 5 nm/min at a substrate temperature of 400°C (supplementary) [65]. The estimated concentration was between 5.5 to 6.5 x10^{20}/cm^3 and the passive film loss was ≤ 0.1dB/cm at 1.61 μm. Subsequently, the device was characterized with the pump at 1.61 μm. The experimental setup is shown in Fig. 2a. The laser was coupled through a lens into the pump channel of the fiber WDM which was fusion spliced to a lensed fiber having 3 μm spot size. The signal was around 1.85 μm filtered from a supercontinuum source (NKT Fiannium) with a bandpass filter which was launched into the signal channel of the WDM. The coupling loss for the signal and the pump was between 2.5-2.8 dB/facet and 3.5 dB/facet, respectively. In the experiment, we used co-propagating pump and signal due to ease of operation; however, counterpropagating scheme can equally be implemented as not much difference between the two schemes in the experiment was observed (supplementary). This is due to fact that the amplified spontaneous emission (ASE), which usually takes away the gain from a small signal, depending on the direction of pumping, is dominated by the strong seed signal used in this work [66]. The chip was mounted on a thermally conductive tape for stable operation at high power. The signal was collected at the output with a lensed fiber connected to a WDM which was, down the line, connected through an attenuator to a calibrated optical spectrum analyzer and

a power meter. The on-chip amplified signal power at the output and the net gain as a function of pump power are shown in Fig. 2c, and d, respectively. In this report, the stated optical power is the on-chip power, unless otherwise stated. Output signal power reached close to 1 W amounting to ~14.5 dB net gain for an input signal power of ~36 mW (maximum signal limited by the source). Upto 16.5 dB net gain was seen for signal around 18 mW before parasitic lasing occurred as shown later. The conversion efficiency at the maximum output ranges between 63-66% (taking into account uncertainity in the pump power coupling). The amplifier was also tested at lower signal power as shown in Fig. 3. The signal ranged from <0.1 mW to ~ 36 mW and the pump was varied from 140 mW to 1.48 W. The green shaded region depicts parasitic lasing region from facet reflection which caused gain clamping. This is mainly because the signal amplification overcomes the roundtrip loss leading to lasing, such phenomenon is a well-known nuisance in amplifiers [42, 44, 67].

The maximum net gain achieved was around 16.5 dB before parasitic lasing sets in, which can be avoided with angled inverse tapers (in a standalone device), high power index matching glue [68], or it can be avoided altogether in a photonic circuitry where the amplifier will be seamlessly connected to other photonic components without strong Fresnel reflection. The gain is the highest when the pump and signal are in the same polarization, which is ensured with the help of waveplates and polarization controller. The input and amplified output signal polarizations were measured to be the same with an extinction ratio of 35 dB at the input and output. By plotting the net gain with respect to the signal power (for the on-chip pump power >0.6W, not shown), the gain saturation power can be estimated to be between 50-90 mW (the signal power for which gain drops to half of its small-signal value), which corresponds to an approximate saturation energy of 35-63 μJ for an upperstate lifetime of 700 μs.

To study the luminescence properties of the active ions in the gain film we perform photoluminescence (PL) measurements. In order to avoid effects such as, reabsorption, ASE and wavelength dependent loss of the waveguide, we coupled the pump into the waveguide with end-fire coupling and collected the PL with an out-of-plane collection setup (see method and supplementary for details). The measured upperstate lifetime for the TM mode at low power was 1 ms, which dropped to 720 μs for high pump power (>300 mW) due to energy transfer up conversion processes [62, 69-71]. Similar measurements were performed for the signal and pump in TE mode having a larger mode area (<60 μm^2). A slightly shorter lifetime was measured for the larger TE mode, ~ 660 μs at higher pump power. We also compared the PL strength of the two modes (Fig. 4a), and we observed that the larger mode gave stronger PL, which is mainly due to exciting a large number of ions, suggesting a higher gain for the larger mode (we note that the peak of the PL is around 1830 nm unlike the gain (at 1850 nm), that is due to lower absorption loss at 1850 nm). The shape of the PL spectra from the TE and TM mode remained the same except varying in strength for the measured pump power. The simulated mode profiles of the two modes, TE and TM, are shown in Fig. 4b, and the pump and the signal mode overlap is over 98% for both polarizations. The group index is 1.75 and 1.77 for the TE and TM mode, respectively. The gain was measured for the TE mode and the difference in gain between the TE and TM mode at different pump powers is shown in Fig. 4b (for an on-chip signal power of ~ 18 mW). The TE mode gain gradually increases with the pump power and surpasses the TM gain around 0.4 W of pump power. At

higher pump power the TE mode experienced parasitic lasing, which is mainly due to the high gain for the TE mode, which is related to strong photoluminescence for the TE mode and the fact that a larger optical mode leads to a higher gain saturation power; but the effect of stronger interaction with the inhomogeneities in the film cannot be ruled out (causing localized index variation and lifetime variations between TE and TM modes) [72, 73]), which can enhance backscattering and induce early onset of parasitic lasing [74]. This behavior can be avoided by improving the film quality which is sensitive to initial deposition conditions [72]. Nevertheless, this demonstrates that even a larger mode reaching the level of a single mode fiber is achievable without incurring high losses. Thus, a smaller amplifier with high energy storage is foreseeable and will be the

subject of future device optimization.

Next, we measured the relative intensity noise (RIN) introduced by the amplifier with a signal-source-analyzer (which was locked at the repetition rate of the signal, 78 MHz), see method for details. The noise spectrum at the offset frequency ~ 0.8 kHz and beyond from the carrier is shown in Fig. 4c. We launched the signal with power > 30 mW and varied the pump power from 180 mW to 1.1 W. The input signal noise is already high as we use the filtered long wavelength edge of the supercontinuum, which is known to have high amplitude noise due to amplified input shot noise through nonlinear processes and spontaneous Raman scattering in the PCF fiber [75]. From a few kHz to several hundred kHz the RIN drops below the input noise, which is due to the high pass filtering effect of the gain with respect to the signal noise [76-78]. This is because the gain is unable to react to the amplitude modulation in the signal (due to noise) below the cut-off frequency (which increases linearly with the output signal power up to the point where the residual pump power starts to increase). In Fig. 4c we see that the curve is shifting to higher cut-off frequencies with the input pump power up to the point where residual pump power at the output starts to increase which is around > 0.85 W of pump power. That is because as the residual pump power increases, the low frequency component of noise from the pump starts to dominate because the gain (population inversion) acts as a low pass filter for the pump fluctuation [76, 77]. Due the same reason in the sub-kHz range (not shown) the noise is dominated by the pump amplitude noise. We have also measured the RIN at different signal power (above parasitic lasing threshold) at a fixed pump power, as shown in Fig. 4d. The noise increased from high power to low power input signal by <0.4 dB, which is due to the gradual increase in ASE power as the signal power drops. The noise performance is better than a clad pumped LMA fiber high power amplifier for a similar gain system, most likely because our device operates with single fundamental mode, avoiding excitation of ASE in the higher order modes as is the case with LMA fiber amplifiers [44, 79]. Additionally, we have measured the noise figure (with a home-built CW laser) to be between 4 to 5 dB for an on-chip seed power of 36 mW and a net gain of ~ 15 dB, see supplementary.

In conclusion, we have demonstrated the first high power amplifier on a CMOS compatible integrated photonics platform with watt-level output power within a footprint of only ~ 4.4mm^2. The LMA waveguide demonstrated here is a broadband device and as mentioned above is not limited to any specific foundry and therefore can easily be adapted to different spectral windows limited only by the

material absorption (for example thin silicon nitride layer for short wavelength applications can be utilized). Moreover, the mode area exploited here was around 30 μm^2 and even larger modes (60 μm^2) were demonstrated with low loss, suggesting that even higher power with even larger mode area and more compact amplifiers can be achieved. For example, reaching mode areas to the level of LMA fiber (>500 μm^2) to allow even higher power. Moreover, by coherently combining signals from many such amplifiers on a single CMOS die, one can get over a 100 watts of output power from a single chip as they can accommodate many such amplifiers. Polarization independent gain can be achieved with appropriately designed amplifiers or with a polarization diversity scheme seamlessly integrated with the amplifier [80, 81]. Moreover, pulses can be amplified to very high energy, especially in combination with chirped pulse amplification (CPA) using apodized chirped gratings already demonstrated [82]. Such LMA based high power amplifiers and lasers in the 2 μm window will prove quite beneficial for commercial and scientific applications. For example, small satellites for earth and planetary sciences, especially, the small size and weight CubeSat lidars, can be used for greenhouse gas monitoring, such as CO_2 and H_2O detection and mapping, which are also essential for detecting signs of life on other planets [20, 83]. Due to strong water absorption, lasers operating around 1.9 μm are being used for medical surgeries, where miniaturization of these systems is highly desired for wider accessibility [84-86]. Moreover, it is estimated, that next generation gravitational wave detectors will have an increased detection range by five times, when silica-based mirrors are replaced with silicon mirrors that suffer less from thermal noise [87]. High transparency of silicon at 2 μm makes the thulium-based lasers appropriate for such upgrades, especially the future space-based gravitational observatories which will benefit from millimeter scale high power lasers. Similarly, optical frequency synthesizer with all silicon components will require long wavelength lasers for second harmonic generation in silicon where multiphoton absorption is weak [13, 88], enabling self-referencing for stable comb generation with all CMOS circuitry for applications in optical atomic clocks, coherent telecommunication and microwave photonics. Scaling to other important wavelength windows is also straight forward, for example, 1 μm for high power applications with ytterbium ions, 1300 nm for data center applications with neodymium ions, and 1550 nm for telecom applications with erbium ions. Together with the integration of pump diodes [89], discussed further in the supplementary, the CMOS compatible LMA waveguide technology is poised to broaden the integrated photonics application landscape significantly beyond today’s imagination.

Methods

Fabrication: The passive section was fabricated in LIGENTEC. The photonic layer stack as mentioned above consists of a layer of silicon, bottom silicon dioxide, silicon nitride, top silicon dioxide, aluminum oxide. The sidewall angle of the etched SiN waveguide is measured by LIGENTEC to be 89° and the standard variation in SiN thickness and refractive index was ±5%, and ±0.25%, respectively. Silicon substrate thickness = 230 μm, bottom oxide thickness = 4 μm and the top oxide thickness = 3.3 μm. Following the patterning of the SiN layer a silica layer was deposited which was subsequently etched away (to create the gain deposition window, Fig.1c) up to the point where the silica was 310nm thick on top of the SiN layer - this is the interlayer oxide. SiN fill patterns were fabricated to maintain high enough

density of SiN (>20%) across the die to avoid fabrication complications. The gain layer was deposited at the University of Twente with an RF sputtering tool (details in the supplementary). The chip was mounted in a holder and is loaded into an AJA ATC 15000 RF reactive co-sputtering system through a load-lock and is placed on a rotating holder in the main reaction chamber. A two-inch aluminum target (99.9995% purity) and thulium target are powered through their own RF sources. A power of 200 W is used on the aluminum target and 21 W is used on the thulium target which determines the ion concentration in the film. The expected deposition temperature was around ~400°C and the rate of deposition was around 4 to 5 nm/min which varies by ± 1nm from run to run. After the deposition the samples film quality was characterized with a prism coupling tool (Metricon 2010/M).

Spectroscopic measurements: For the upperstate lifetime measurement (see supplementary for details), the device was optically pumped by an amplified low noise CW laser (Alnair labs, TLG 220). We used a high-power polarization maintaining L-band amplifier (IPG EAR-10-1610-LP-SF). The same pump was used for amplifier testing. The pump laser goes through a free space setup (consisting of two collimating lenses with a 20 cm free space in between and a chopper was placed in between). The pump was edge coupled to the waveguide and a multimode fiber (Thorlab - M43LO2) coupled light out with an out-of-plane setup. Subsequently, the signal goes through a free space setup: with a lens collimator, bandpass filter (Thorlab FB 1900-200) to remove the residual pump, focusing lens on to a fixed gain amplified InGaAs detector (Thorlab PDA-10D2), which went to an oscilloscope (RS pro RSDS 1304 CFL) through a 20 KHz low noise low pass filter (Thorlab EF-120). For measuring the PL light the pump was launched into the gain layer and the out-of-plane multimode fibre collected the PL light which went straight into the OSA. We note that the PL spectrum was also measured with the 790 nm pump (not shown), and the spectrum was similar to the one obtained with 1.61 μm pumping.

RIN measurement: The signal and the pump were coupled into the chip as shown in Fig. 1. At the output the signal port of the WDM goes through a free space setup (two collimating lenses coupled to single mode fibers with a 20 cm long free space in between the lenses) in which a bandpass filter to remove pump light was placed. The signal was further attenuated with a variable attenuator to avoid detector saturation (Thorlab VOA-50FC/APC). The light was detected with an InGaAs 12 GHz detector (EOT ET 5000 F/APC), which goes through a bandpass filter (41 – 120 MHz), to detect the signal around 78 MHz (repetition rate of the NKT signal source), which goes through a low noise amplifier ZX60-33LN-S+ (mini circuit) and then into a signal source analyzer to measure the AM noise (SSA-E5052B).

Refractive index: The optical constants of the Al_2O_3 film were measured with a VASE ellipsometer (J.A. Woollam Co.) covering the wavelength range from 240 nm to beyond 11 μm (see supplementary for details). To isolate the influence from to the silicon and silica substrates, samples with only oxidized silicon and bare silicon were also measured**.** The refractive index at 1.9 μm of the film was measured to be ~ 1.7.

Declarations

Acknowledgements:

This work is supported by DESY, a center of the Helmholtz Association through the MML-Programme in POF IV and Maxwell Computing platform, the EU Horizon 2020 Framework Programme - Grant Agreement No.: 965124 (FEMTOCHIP), and Deutsche Forschungsgemeinschaft (SP2111) contract no. 403188360.

Competing interest:

The authors declare no competing interests.

Data availability:

All the relevant code and data supporting this study are available from the corresponding author on reasonable request.

Author contributions:

N.S. originally conceived and conceptualized the LMA amplifier and subsequently designed and tested it. J. L. helped in the testing. K. W. and S.M.G.B. deposited the gain film on the amplifier chip. H. F. and M.G. fabricated the chip. M. S, M. G. and T. H., helped in editing the manuscript. M. E. helped with the RIN measurements. F. X. K. initiated and supervised the project. All authors helped in writing the manuscript.

References

1. A. E Willner et. al., “Optics and Photonics: Key Enabling Technologies,” *Proc. IEEE*, 100 (2012).
2. Wei Shi et. al., “Fiber lasers and their applications,” *Appl. Opt.*, 53 (2014).
3. D. J. Richardson et. al., “High power fiber lasers: current status and future perspectives,” *JOSA B,* 11 (2010).
4. M. N. Zervas and C. A. Codermard, “High Power Fiber Lasers: A Review,” *IEEE J. Sel. Top.,* 20 (2014).
5. C. Jauregui et. al., “High-power fibre lasers,” *Nat. Photonics*, 7 (2013).
6. A. Cingoz et. al., “Direct frequency comb spectroscopy in the extreme ultraviolet,” *Nature*, 482, (2012).
7. T. R. Schibli et. al.,“ Optical frequency comb with submillihertz linewidth and more than 10 W average power,” *Nat. Photonics* 2, (2008).
8. K. Sugioka and Y. Cheng, “Ultrafast laser – reliable tools for advanced materials processing,” *Light Sci. Appl*. 3, (2014).
9. X. Zhang et. al., “A large scale microelectromechanical systems bases silicon photonic LiDAR,” Nature, 603 (2022).
10. Z. Li. et. al., “Thulium-doped fiber amplifier for optical communications at 2 μm,” *Opt. Express*, 21 (2013).

11. P. D. Haye et. al.,"Phase coherent microwave to optical link with a self-referenced microcomb," *Nat. Photonics,* 10 (2016).
12. D. T. Spencer et. al., "An optical frequency synthesizer using integrated photonics," *Nature*, 557 (2018).
13. N. Singh et. al., "Silicon photonics optical frequency synthesizer," *Laser Photonics Rev.* 14 (2020).
14. www.seminex.com "Seminex unveils high gain optical amplifiers for LIDAR" *Seminex news* (2022). S. Aboujja et.al., "High performance semiconductor optical amplifier and array for FMCW LiDAR in high speed autonomous vehicles," *SPIE LASE*, 12403 (2023).
15. www.lumentum.com, E. Canoglu et. al. "Semiconductor lasers and optical amplifiers for LiDAR photonic integrated circuits," *International semiconductor laser conference*, 21531815 (2021).
16. J. M. Dailey et. al., "High output power laser transmitter for high efficiency deep space optical communications," *SPIE LASE,* 109100M (2019).
17. D. M. Cornwell "NASA's optical communications program for 2017 and beyond," *IEEE ICSOS* (2017).
18. H. Hemmati et. al., "Deep-Space Optical Communications: Future Perspectives and Applications," *Proc. IEEE*, 99 (2011).
19. H. Kaushal, and G. Kaddoum, "Optical communication in space: challenges and mitigation techniques," *IEEE commun. Surv Tutor.,* 19 (2017).
20. O. Graydon, "Conquering the final frontier," Nat. Photonics, 12 (2018).
21. P. W. Juodawlkis et. al., "High-Power, Low-Noise 1.5-μm Slab-Coupled Optical Waveguide (SCOW) Emitters: Physics, Devices, and Applications," *IEEE J Sel Top Quantum Electron*, 17 (2011).
22. H. Zhao et. al., "High power indium phosphide photonic integrated circuits," *IEEE J. Sel. Top.* 25, (2019).
23. M. L. Davenport et. al., "Heterogeneous Silicon/III–V Semiconductor Optical Amplifiers," *IEEE J. Sel. Top.*, 22 (2016).
24. K. V Gasse et. al., "27 dB gain III-V on silicon semiconductor optical amplifier with >17 dBm output power," *Opt. Express*, 27 (2019).
25. Z. Zhou et. al., "On-chip light sources for silicon photonics", *Light Sci. Appl*. 5 (2015).
26. J. Kenyon, "Erbium in silicon", *Semicond. Sci. Technol.*, 20 (2005).
27. H. Ennen et. al. "1.54 - μm luminescence of erbium-implanted III-V semiconductors and silicon," Appl. Phys. Lett 43, 10, (1983).
28. W. T. Tsang and R. A. Logan, "Observation of enhanced single longitudinal mode operation in 1.5um GaInAsP erbium-doped semiconductor injection laser," Appl. Phys. Lett, 49 (1986).
29. Purnawirman, et. al., "C- and L-band erbium-doped waveguide lasers with wafer-scale silicon nitride cavities," *Opt. Lett*. 38 (2013).
30. L. Agazzi, et. al., "Monolithic integration of erbium-doped amplifiers with silicon-on-insulator waveguides," *Opt. Express,* 18 (2010)

31. M. Belt and D. J. Blumenthal, “High temperature operation of an integrated erbium- doped DBR laser on an ultra-low-loss Si3N4 platform,” *OFC* paper Tu2C.7 (2015)
32. E. S. Magden et al., "Monolithically-integrated distributed feedback laser compatible with CMOS processing", *Opt. Express*, 25 (2017).
33. N. Li et al., "Monolithically integrated erbium-doped tunable laser on a CMOS-compatible silicon photonics platform", *Opt. Express*, 26 (2018).
34. J. Rönn et al., "Ultra-high on-chip optical gain in erbium-based hybrid slot waveguides", *Nat. Commun.*10 (2019).
35. H. Sun et al., "Giant optical gain in a single-crystal erbium chloride silicate nanowire", *Nat. Photonics,* 11 (2017).
36. A Choudhary et al., "A diode-pumped 1.5 μm waveguide laser mode-locked at 6.8 GHz by a quantum dot SESAM", *Laser Phys. Lett.*, 10 (2013).
37. H. Byun et al., "Integrated low-jitter 400-MHz femtosecond waveguide laser", *IEEE Photon. Technol. Lett*. 21 (2009).
38. J. D. Bradley et. al., "Monolithic erbium- and ytterbium doped microring lasers on silicon chips", *Opt. Express* 22 (2014).
39. K. van Dalfsen et. al., “Thulium channel waveguide laser with 1.6 W of output power and ~80% slope efficiency,” *Opt. Lett.* 39 (2014).
40. K. Shtyrkova et. al., "Integrated CMOS-compatible Q-switched mode-locked lasers at 1900 nm with an on-chip artificial saturable absorber", *Opt. Express*, 27 (2019).
41. F. X. Kärtner et.al.,“Integrated CMOS-compatible mode-locked lasers and their optoelectronic applications”, *Proc. SPIE 10686*, 14 (2018).
42. Y. Liu et. al., “A photonic integrated circuit based erbium doped amplifier,” *Science*, 376 (2022).
43. D. Taverner et. al., “158-uJ pulses from a single-transverse-mode, large-mode-area erbium-doped fiber amplifier,” *Opt. Lett.,* 22 (1997)
44. C. C. Renaud et. al., “Characteristics of Q-switched cladding-pumped ytterbium-doped fiber lasers with different high-energy fiber designs,” *IEEE J. Quantum Electron.* 27 (2001)
45. J. Limpert et. al., “100-W average power, high-energy nanosecond fiber amplifier,” *Appl. Phys. B*, 75 (2002).
46. M. Y. Cheng et. al.,“ High-energy and high-peak-power nanosecond pulse generation with beam quality control in 200-μm core highly multimode Yb-doped fiber amplifiers,” *Opt. Lett* 30 (2005).
47. N. Volet, et. al. “Semiconductor optical amplifier at 2 μm wavelength on silicon,” *Laser Photonics Rev.* 11, 2017.
48. N. Singh et.al. “Towards CW modelocked laser on chip – a large mode area and NLI for stretched pulse mode locking”, *Opt. Express*, 28 (2020).
49. N. Singh et. al., “Silicon photonics based high energy passively Q switched laser,” *Nat. Photonics.* (2024).

50. www.advaluephotonics.com. Advalue photonics - 2 Micron Fiber amplifier (Ap-Amp).
51. www.thorlabs.com. PicoLuz – Thulium doped fiber amplifier.
52. S. J. Choi, et. al. “Microdisk lasers vertically coupled to output waveguides,” IEEE PTL, 15 (2003)
53. A. W. Fang et. al. “Electrically pumped hybrid AlGaInAs-silicon evanescent laser,” Opt. Express, (2006).
54. J. V. Campenhout et. al. “Electrically pumped InP-based microdisk lasers integrated with a nanophotonic silicon on insulator waveguide circuit,” Opt. Express, 15 (2007).
55. H. W. Chen et. al. “A hybrid silicon AlGasInAs phase modulator,” IEEE PTL, (2008).
56. M. Belt, et. al. “Arrayed narrow linewidth erbium-doped waveguide-distributed feedback lasers on an ultra-low-loss silicon-nitride platform” Opt. Lett (2013).
57. K Scholle et al., “2 μm Laser Sources and Their Possible Applications,” *Frontiers in guided wave optics and optoelectronic*s, 2010.
58. K. Yang et. al., “Q-Switched 2 micron solid-state laser and their applications,” *Frontiers in guided wave optics and optoelectronics*, 2019.
59. C. Boone, “Medical applications are a surgical fit for 2 μm lasers,” *Laser Focus World*, 2022.
60. X. Xie et. al., “A brief review of 2 μm laser scalpel,” *IEEE 5th Optoelectronics,* 2022.
61. U. N. Singh, “Progress on high energy 2 micron solid state laser for NASA space-based wind and carbon dioxide measurments,” 011 *IEEE SUM*, 2011.
62. A. Sincore et. al., “High average power thulium-doped silica fiber lasers: review of systems and concepts,” *IEEE J. Sel. Top*. 24 (2018).
63. M. Lenski et. al., “Inband-pumped, high power thulium doped fiber amplifiers for an ultrafast pulsed operation,” *Opt. Express*, 24 (2022)
64. G. D. Goodno et. al., “Low-phase-noise, single-frequency, single-mode 608 W thulium fiber amplifier,” *Opt. Lett.* 34 (2009)
65. C. I. van. Emmerik, et. al., “Relative oxidation state of the target as guideline for depositing optical quality RF reactive magnetron sputtered Al_2O_3 layers,” *Opt. Mat. Express,* 10 (2020).
66. P. C. Becker, N. A. Olsson and J. R. Simpson, “Erbium-doped fiber amplifiers,” Academic Press 1999.
67. D. C. Brown et. al., “Parasitic oscillations, absorption, stored energy density and heat density in active-mirror and disk amplifiers,” *Appl. Optics*, 17 (1978).
68. http://www.luvantixadm.com
69. D. A. Simpson et. al., “Energy transfer up-conversion in Tm3+ - doped silica fiber,” *J. Non-Cryst.* 352 (2006).
70. G. Nykolak et. al., “Concentration-dependent $^4I_{13/2}$ lifetimes in Er^{3+} doped fibers and Er^{3+} doped planar waveguides,” *IEEE Photonic Tech L*. 5 (1993).
71. K. Kuroda et. al., “Pump-probe measurment of metastable state lifetime reduced by cooperative upconversion in a high-concentration erbium doped fiber,” *Appl. Opt.* 57 (2018).

72. R. A. Gardner et. al., “Stability of RF-sputtered aluminum oxide”, *JVSTA*, 14 (1977).
73. F. Hacker et. al., “RF-sputterd SiO_2 films for optical applications,” *Thin Solid Films*, 97 (1982).
74. A.A. Hardy and R. Oron, “Amplified spontaneous emission and Rayleigh backscattering in strongly pumped fiber amplifiers,” *J. Light. Technol.* 16 (1998).
75. K. L. Corwin et. al., “Fundamental noise limitations to supercontinuum generation in microstructure fiber,” *Phys. Rev. Lett.* 90 (2003).
76. S. Novak and A. Moesle, “Analytic model for gain modulation in EDFAs,” J. Light. Technol. 20 (2002).
77. H. Tunnermann et. al., “Gain dynamics and refractive index changes in fiber amplifiers: a frequency domain approach,” *Opt. Express.* 20 (2012).
78. J. Zhao et. al., “Gain dynamics of clad-pumped Yb-fiber amplifier and intensity noise control,” *Opt. Express*, 25 (2017).
79. G. Guiraud et. al., “High power and low intensity noise laser at 1064nm,” *Opt. Lett.* 41 (2016).
80. T. Barwicz, et. al. “Polarization-transparent microphotonic devices in the strong confinement limit,” Nat. Photon. 1, (2007).
81. D. Dai and J. E. Bowers, “Novel concept for ultracompact polarization splitter-rotator based on silicon nanowires,” Opt. Express. 19 (2011).
82. M. Sinobad et. al., “Apodized chirped Bragg gratings in a silicon nitride-on-insulator platform at short-wave infrared wavelengths,” CLEO EU (2023).
83. M. Storm et. al, “Cubesat lidar concepts for ranging, topology, sample capture surface and atmospheric science,” Small Satellite conference (2017).
84. K Scholle, et al. “2 µm Laser Sources and Their Possible Applications,” *Frontiers in guided wave optics and optoelectronic*s, (2010).
85. A. Schliesser et. al. “Mid infrared frequency combs,” Nature Photonics (2012).
86. N. M. Fried and P. B. Irby “Advances in laser technology and fibre-optic delivery systems in lithotripsy”, Nat. Rev. Urol, 15 (2018).
87. D. P. Kapasi et. al. “Tunable narrow-linewidth laser at 2um wavelength for gravitational wave detector research,” Opt. Express, 28 (2020).
88. N. Singh et. al. “Octave-spanning coherent supercontinuum generation in silicon on insulator from 1.06 µm to beyond 2.4 µm,” Light. Sci. Appl. 7 (2018).
89. M. Theurer et. al., “Flip-chip integration of InP to Sin photonic integrated circuits,” *J. Light. Technol.* 38 (2020).

Figures

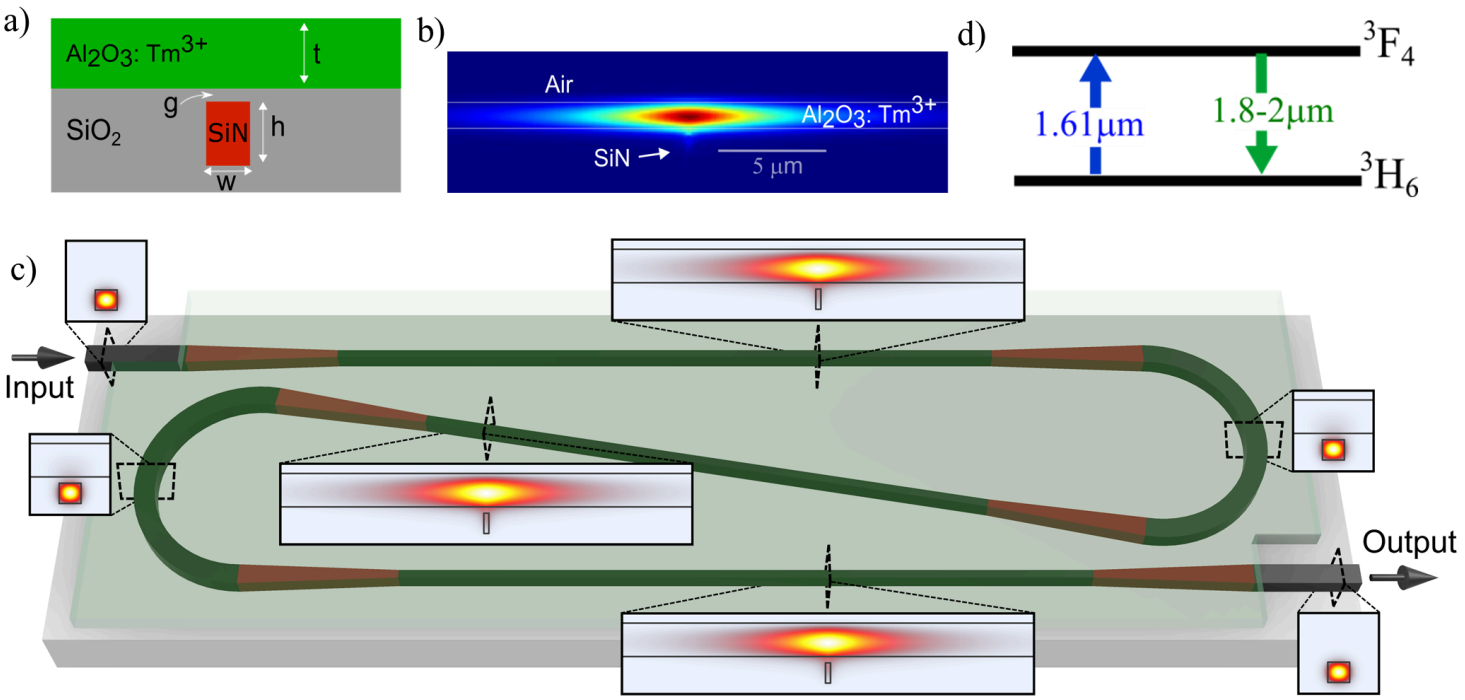

Figure 1

a) The LMA waveguide cross-section, where *t* is the thickness of the gain film (>1.35 μm), *g* is the thickness of the interlayer oxide (310 nm), *h* and *w* are the height (800 nm) and width (280 nm) of the SiN layer. b) The signal mode profile at 1.85 μm, with an A_{eff} ~ 30 μm^2. c) The amplifier schematic, in which the pump and the signal are launched from the input side and the amplified signal is collected at the output. The small modes around the bends indicate the tight confinement region where the mode is well confined within the SiN layer. The images of large mode indicate the LMA region where the pump excites the gain ions to the upper state to amplify the co-propagating signal. The brown sections indicate the adiabatic tapers to transition the large modes back to the tight modes to allow for tighter bends. d) A simplified energy diagram of thulium doped alumina with the pump at 1.61 μm and the signal ranging from 1.8 to 2 μm.

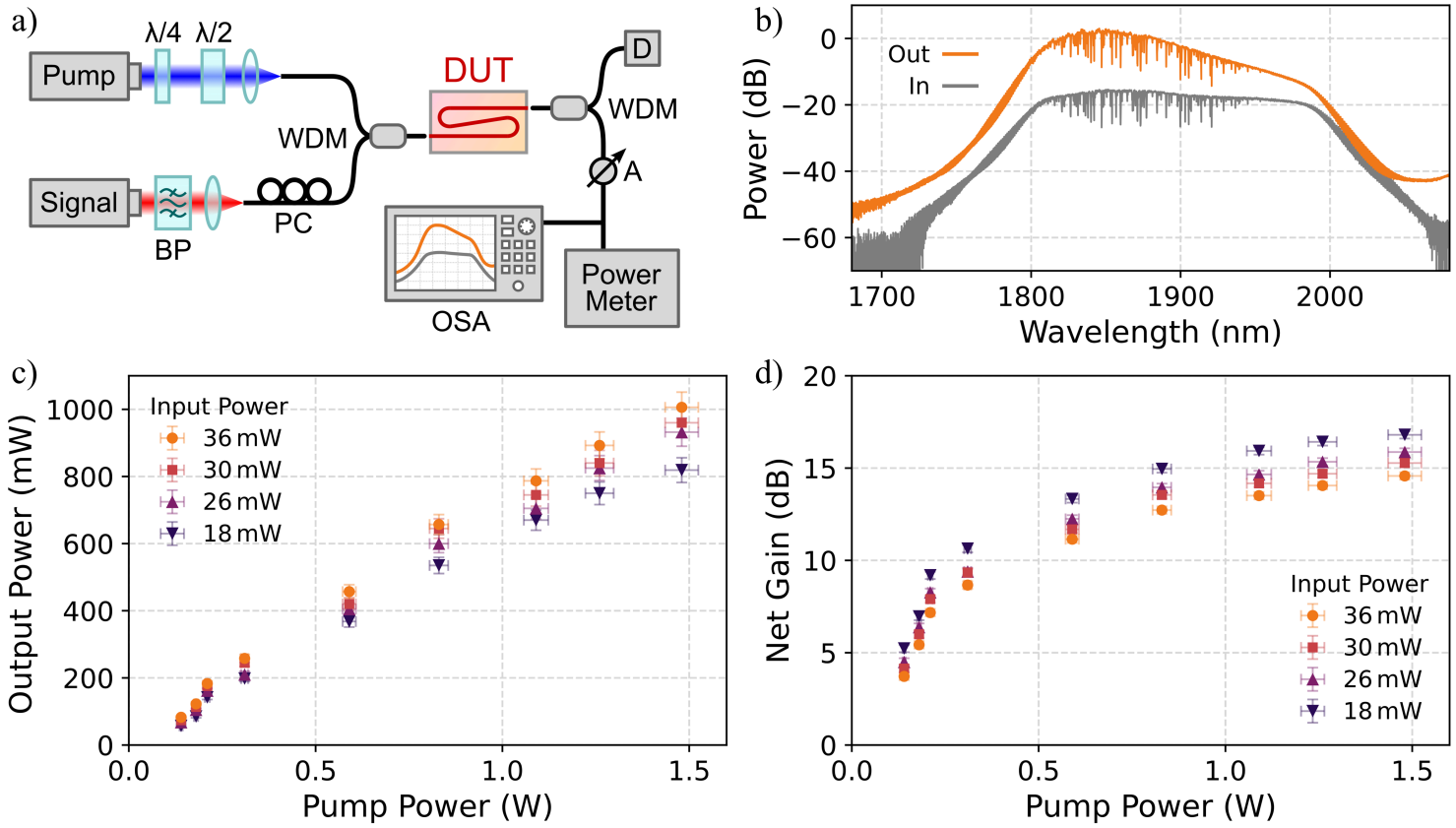

Figure 2

a) The experimental setup. BP is a bandpass filter, PC is a polarization controller, WDM is a wavelength division multiplexer, D is a pump dump, A is a variable attenuator and DUT is the device under test. b) Spectra of input signal and amplified output signal. c) On-chip output signal power as a function of pump power for on-chip signal power ranging from 18 mW to 36 mW. d) The net on-chip gain as a function of pump power.

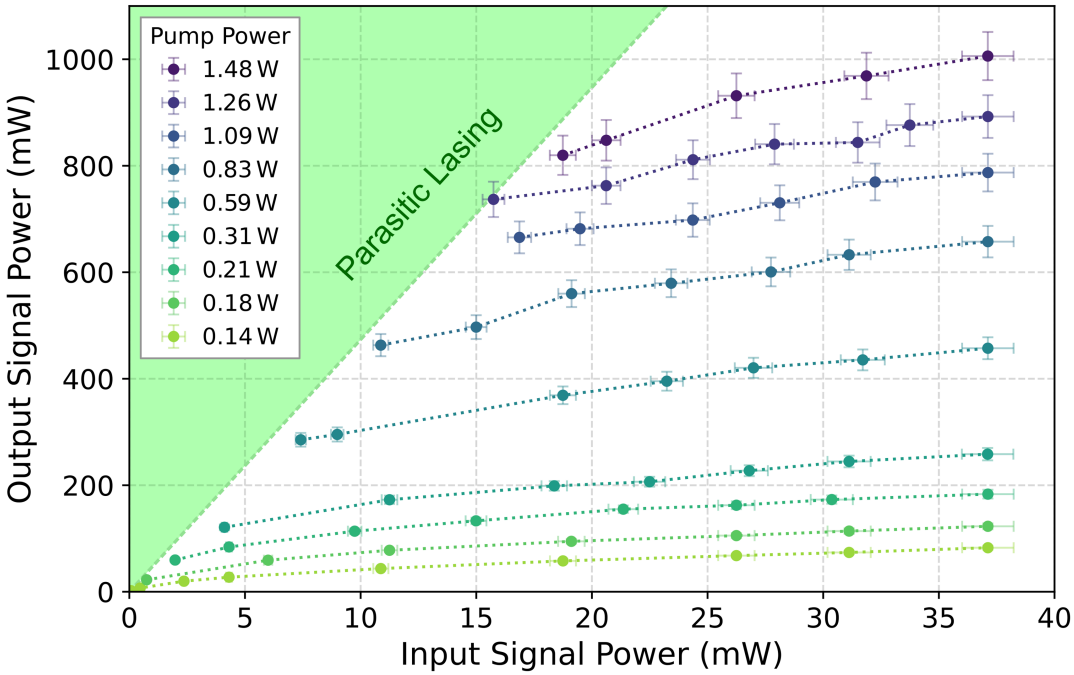

Figure 3

On-chip output signal power as a function of on-chip input signal power at different pump power levels. The green shadowed region depicts the region of parasitic lasing. The dashed lines connecting the data points are guides for the eye.

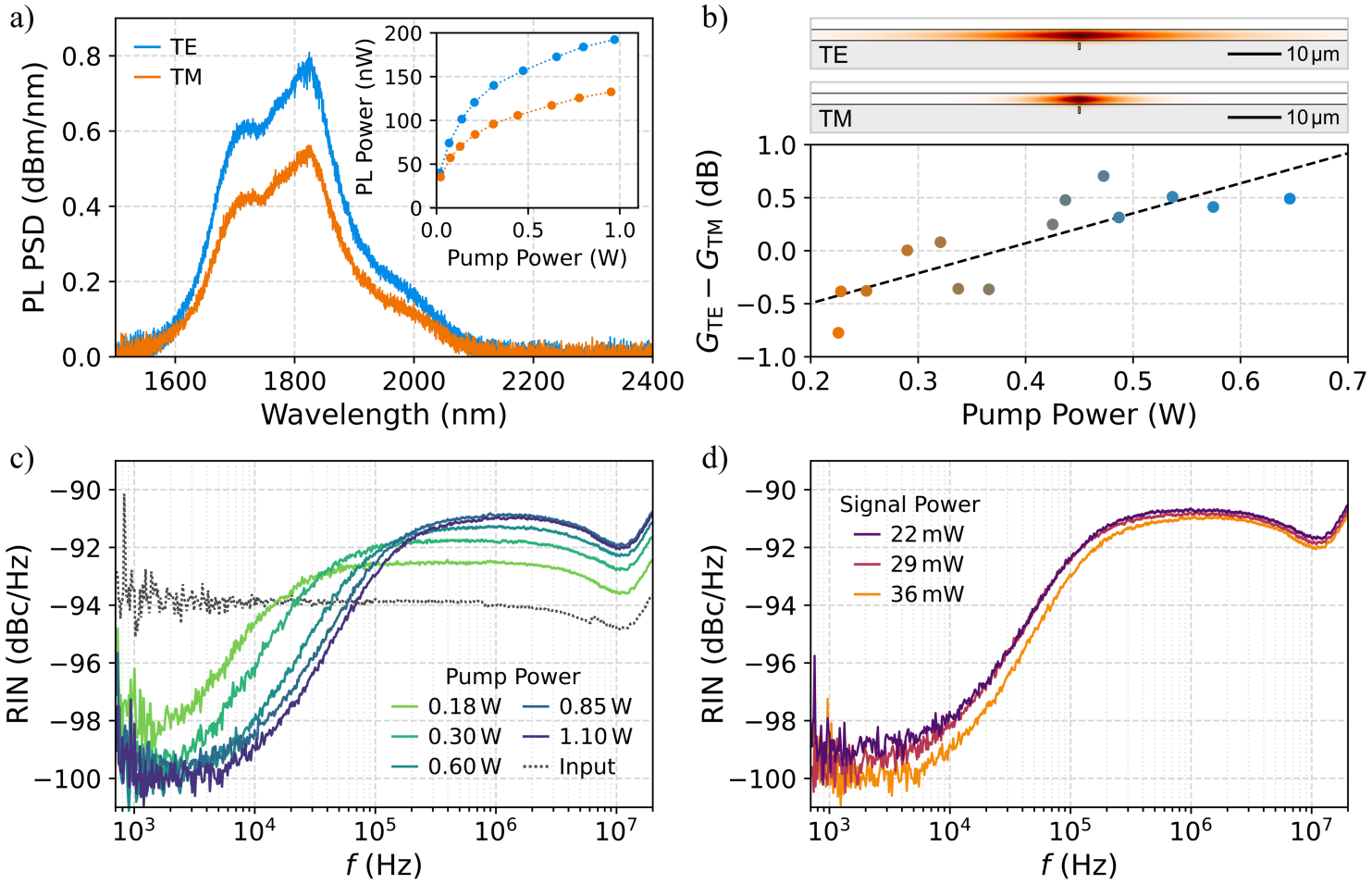

Figure 4

a) The PL power spectral density (PSD) curves of the TE and TM modes taken at 950 mW pump power, along with the integrated PL power with respect to the pump power (inset). b) The mode profiles of the TM mode and the TE mode, and the difference between the measured net gain between the two (the straight dashed-line is the linear fit to the data). c) RIN of the output signal at different pump power. The dashed curve is the RIN of the reference signal. d) The RIN of the signal for different input signal power at a fixed pump power of 1.1 W.

Supplementary Files

This is a list of supplementary files associated with this preprint. Click to download.

- SupplementaryFinalNPv21.docx